Journal of Materials Chemistry C

ROYAL SOCIETY OF CHEMISTRY

PAPER

View Article Online
View Journal | View Issue

Cite this: J. Mater. Chem. C, 2025, 13, 2238

Sensitized near-infrared lanthanide emission in chalcogenide perovskites†

Jinan H. Al Shuhaib, [a] Isabel J. Ferrer, [ab] José R. Ares, [a] Salvatore Cianci, [c] Federico Tuzi, [c] Elena Blundo, [c] Antonio Polimeni, [c] Antonio Benayas, [abd] Riccardo Marin *[abde] and Fabrice Leardini *[ab]

Received 17th October 2024,
Accepted 27th November 2024

DOI: 10.1039/d4tc04446k

rsc.li/materials-c

Semiconductor materials capable of hosting luminescent lanthanide ions (Ln^{3+}) and sensitize their emission are scarce. Halide perovskites are prime systems for this purpose, yet they often feature toxic elements (*e.g.*, lead) in their composition and have reduced stability. The discovery of alternative semiconductors that feature host-to-Ln^{3+} energy transfer mechanisms – while being more stable and environmentally benign – would thus broaden the applicability of this class of luminescent materials. Herein, we report near-infrared (NIR) emitting phosphors made of $BaZrS_3$ chalcogenide perovskite doped with Ln^{3+} ions (Ln = Yb, Er, Nd). We chose $BaZrS_3$ because it features (i) crystallographic sites that can accommodate Ln^{3+} ions, (ii) high light absorption coefficient in the visible, and (iii) stability. The phosphors were prepared *via* sulfurization of Ln^{3+}-doped $BaZrO_3$ microparticles obtained by a microwave-assisted procedure. The so-obtained Ln^{3+}-doped $BaZrS_3$ display low-temperature NIR emission characteristic of each Ln^{3+} ion when exciting the matrix. Following photoluminescence studies on doped and undoped $BaZrS_3$ as a function of temperature, we propose an energy level scheme that explains the rich NIR photoluminescence displayed by these phosphors. The obtained results pave the way for the optimization of Ln^{3+}-doped $BaZrS_3$ for optical applications and are expected to spur the study of other ternary chalcogenides sensitization of Ln^{3+} luminescence.

1. Introduction

Lanthanide (Ln^{3+}) ions feature rich 4f energy level schemes that support linear and non-linear photoluminescence with narrow emission lines and long luminescence lifetimes. These properties made Ln^{3+} ions the focus of interest for different photonic applications including bioimaging, luminescence sensing, energy conversion, and anticounterfeiting.[1–3] Yet, Ln^{3+} ions present an important drawback in the context of photoluminescence: an inefficient photon absorption due to the quantum-mechanically forbidden nature of 4f–4f electronic transitions.[4] One approach that has been proposed to circumvent this limitation is the incorporation of Ln^{3+} ions into a semiconductor host matrix that can effectively absorb excitation light and transfer it to the Ln^{3+} emitters (*i.e.*, sensitized emission). However, classical semiconductors (*e.g.*, CdSe, ZnSe, GaN) feature crystal sites with low coordination numbers (CNs = 4). This makes Ln^{3+} incorporation challenging, since these ions prefer CNs $\geq$ 6.[4,5]

Over the past years, halide perovskites (ABX_3, with X = Cl, Br, I) have emerged as state-of-the-art host semiconductor materials to support Ln^{3+} sensitized emission.[5–7] Their success stems from the availability of octahedral B sites (CN = 6) where Ln^{3+} ions can be doped alongside the presence of shallow, localized energy states that have been suggested to support efficient matrix-to-Ln^{3+} energy transfer.[8] However, ABX_3 generally suffer from poor stability, and they often feature Pb^{2+} in their composition (as B element). All in all, there is therefore a limited availability of stable semiconductor materials that can be efficiently doped with Ln^{3+} ions and support their sensitized emission.

More recently, the sensitization of Ln^{2+} photoluminescence from chalcogenide perovskites has been reported. Specifically, visible light emission from Eu^{2+}-doped $SrHfS_3$ has been demonstrated both in powder[9] and in thin films.[10] These demonstrations open alluring prospects, since chalcogenide perovskites present some advantages over halide perovskites, such as non-toxicity and robust stability.

In this work, we expand the scope of the research on Ln^{3+}-doped semiconductors introducing a new family of near-

[a] Departamento de Física de Materiales, Universidad Autónoma de Madrid, E-28049 Madrid, Spain. E-mail: riccardo.marin@uam.es, fabrice.leardini@uam.es
[b] Instituto Nicolás Cabrera, Universidad Autónoma de Madrid, E-28049 Madrid, Spain
[c] Dipartimento di Fisica, Sapienza Università di Roma, I-00185, Rome, Italy
[d] Nanomaterials for Bioimaging Group (nanoBIG), Universidad Autónoma de Madrid, E-28049 Madrid, Spain
[e] Institute for Advanced Research in Chemistry (IAdChem), Universidad Autónoma de Madrird, E-28049 Madrid, Spain

† Electronic supplementary information (ESI) available. See DOI: https://doi.org/10.1039/d4tc04446k

infrared (NIR)-emitting Ln^{3+}-doped sulfide perovskites based on $BaZrS_3$. We start from $BaZrO_3$: a member of the ABO_3 perovskite family, where A is a group II cation (*i.e.*, Ca^{2+}, Sr^{2+}, or Ba^{2+}) in a cuboctahedral site (CN = 12) and B is a group IV transition metal (*i.e.*, Ti^{4+}, Zr^{4+}, or Hf^{4+}) in an octahedral site (CN = 6). Both sites are suitable for hosting Ln^{3+} ions. Yet, in $BaZrO_3$, Ln^{3+} ions preferentially reside at the B site (occupied by Zr^{4+}) with introduction of oxygen vacancies for charge compensation.[1,3,11–13] However, $BaZrO_3$ is an insulator with a direct band gap >3.5 eV, making it a poor visible light absorber.[3,14,15] To push its absorption in the visible range, a CS_2-assisted sulfurization process can be carried out, to obtain the semiconductor material $BaZrS_3$. Here we show that Ln^{3+}-doped $BaZrO_3$ microparticles can be sulfurized *via* this approach, obtaining the first example of NIR luminescent, Ln^{3+}-doped $BaZrS_3$ microparticles. After a thorough spectroscopical, compositional, morphological, and structural characterization, the photoluminescence of the Ln^{3+}-doped $BaZrS_3$ microparticles was investigated as a function of temperature (from 10 K up to room temperature). The semiconductor-sensitized emission of Yb^{3+}, Er^{3+}, and Nd^{3+} was observed and a tentative interpretation of the mechanisms underpinning the optical properties of the microparticles is provided.

2. Experimental details

2.1. Chemicals

Commercial $BaZrO_3$ powders were acquired from Sigma Aldrich. Barium nitrate ($BaNO_3$, 99.95%), zirconyl chloride hydrate ($ZrOCl_2{\cdot}xH_2O$, 99.9%), and lanthanide oxides (Nd_2O_3, 99.9%; Er_2O_3, 99.9%; Yb_2O_3, 99.9%), hydrochloric acid (HCl, 37%) were purchased from Alfa Aesar. Sodium hydroxide (NaOH, >97%) was purchased from Thermo Scientific Chemicals. CS_2 ($\geq$99.5%) used for sulfurization was from Emsure. Ethanol (96%) was purchased from Labbox España.

2.2. Synthesis methods

$BaZrO_3$ (BZO) powders were prepared *via* a microwave-assisted hydrothermal method. The synthesis was performed using a microwave (MW) reactor (CEM Discover 2.0) by adopting a procedure previously reported in the literature.[12] Briefly, 0.5 mmol of $Ba(NO_3)_2$ (130.7 mg) and $ZrOCl_2{\cdot}8H_2O$ (162.1 mg) were added to a 35-mL Pyrex vessel lined with Teflon, along with 10 mL of a 1 M NaOH solution (1 : 1 H_2O : ethanol) and a stirring bar. The pH was adjusted to 10 with additional NaOH solution. After stirring for 30 min at room temperature (sonication was occasionally used to promote dissolution of the salts), the vessel was capped and placed in the MW reactor. The mixture was heated to 200 °C over the course of 10 min (18 °C min^{-1} heating rate approximately), and kept at that temperature for 30 min. After cooling to room temperature, a white precipitate was collected *via* centrifugation (5 min, 3000 rcf) and washed at least 4 times with ethanol to remove unreacted precursors and excess NaOH. The powder was placed in an oven at 60 °C overnight to dry and later crushed in an agate mortar. For Ln^{3+}-doped BZO samples (Ln = Nd, Er, Yb), 2% of the total amount of Zr^{4+} was substituted with the respective Ln^{3+}, using chloride salts as precursors. The following quantities were used: 0.49 mmol $ZrOCl_2{\cdot}8H_2O$ (158.9 mg) and 0.01 mmol of either $NdCl_3{\cdot}6H_2O$ (3.6 mg), $ErCl_3{\cdot}6H_2O$ (3.8 mg), or $YbCl_3{\cdot}6H_2O$ (3.9 mg). Lanthanide chlorides were prepared from the respective oxides, dissolving them in diluted HCl and drying them overnight at 60 °C in an open atmosphere. Undoped and doped BZO powders were calcined at 1000 °C for 3 h, and labelled as BZO, BZO-Nd, BZO-Er, and BZO-Yb (BZO-Ln taken altogether).

Undoped and Ln^{3+}-doped $BaZrS_3$ powders were prepared by sulfurization of the corresponding oxides by using CS_2 as sulfur source according to the approach described in our previous work.[16] Briefly, sulfurization was carried out in sealed silica ampoules (10 mm in diameter, 170 mm in length, and 2.5 mm in wall thickness) at temperatures $\geq$900 °C. Before sulfurization, the ampoules were cleaned by oxygen plasma in a Zepto plasma surface treatment machine (Diener electronic GmbH & Co. KG). The oxide powders were placed at the bottom of the ampoule and CS_2 was added using a Pasteur pipette. All this procedure was conducted inside a glove box (JACOMEX, Model Campus) and an Ar-filled glove bag to prevent introducing oxygen or moisture in the ampoules. The amount of CS_2 was limited to reach a maximum pressure of 10 bar inside the ampoule when heating at high temperatures. The mass of the oxide precursors was kept at approximately 130 mg to ensure an excess of CS_2 after the complete sulfurization of BZO. The ampoules were later evacuated using a diffusion pump to a residual pressure in the range of 10^{-6} mbar and sealed with a blowtorch. The bottom part of the ampoules was immersed in a liquid nitrogen bath to prevent the evaporation of CS_2 during the sealing process. Subsequently, the ampoules were heated in a tube furnace (Carbolite) at different temperatures ranging between 900 and 1100 °C for 6 days and then allowed to cool down naturally. A temperature gradient of about 50 °C was present between both ends of the ampoules. During the cooling process, the CS_2 excess condensed at the cold side of the ampoules. The ampoules were opened in a ventilated hood and the obtained powders were ground in an agate mortar. All samples were stored and handled in air. Sulfurized undoped samples were labelled according to the sulfurization temperature used (in °C units), namely BZS-900 to BZS-1100. Doped sulfides were prepared by sulfurization of BZO-Ln at 1000 °C and were labelled with the name of the dopant element (BZS-Nd, BZS-Er, BZS-Yb; BZS-Ln taken altogether). Note that the undoped BZS series was obtained sulfurizing commercial BZO powders, while the doped BZS powders were obtained from sulfurization of the doped BZO microparticles prepared *via* MW-assisted synthesis.

2.3. Characterization

The crystal structure of the samples was characterized by X-ray Powder Diffraction (XRPD) using a Bruker D8 diffractometer with power settings of 45 kV and 40 mA. Diffraction patterns were recorded with Cu $K\alpha_1$ radiation (λ = 1.5406 Å) using a θ–2θ Bragg–Brentano configuration with a step of 0.02° and

integration time of 2 s. Rietveld refinements were performed using Fullprof Suite software on scans from 10° to 80°.

Chemical composition and morphological characterizations were carried out by energy dispersive X-ray analysis (EDX) with a Quantax system coupled to a scanning electron microscope (SEM) Hitachi S3000 model. EDX spectra and SEM images were acquired with 15 kV accelerating voltage and a working distance of 15 mm at different magnifications ranging from 100× to 6000×.

Raman spectra were recorded at room temperature in a Witec ALPHA 300AR instrument using a confocal microscope with a 100× objective lens (N. A. = 0.9). A green laser with an excitation wavelength of 532.3 nm and a power of 0.2 mW was used.

Thermogravimetric analyses (TGA) were carried out on a Q600-TA instrument. Samples were heated in alumina crucibles from 25 to 1000 °C at a constant heating rate of 10 °C min^{-1} under Ar flow.

A portion of the powders was pressed into pellets with a diameter and thickness of 5 and 1 mm, respectively, by applying a uniaxial stress of 0.75 GPa using a hydraulic cold press. These pellets were used to measure the diffuse reflectance and photoluminescence (PL).

Diffuse reflectance spectra were collected using a PerkinElmer Lambda 1050 UV-vis spectrometer with an integrating sphere.

PL measurements were carried out at variable temperatures between 10 and 290 K in a He closed-cycle cryostat by Oxford Instruments (CCC1104 model). The samples were excited by a laser with wavelength equal to 405 nm (provided by a single frequency single longitudinal mode laser by Integrated Optics) or 532 nm (provided by a single frequency Nd : YVO_4 laser, DPSS series by Lasos), as specified in the text. The laser was focussed by a standard lens resulting in a laser power density equal to 0.8 W cm^{-2}. The luminescence was dispersed by a 75-cm focal length Acton monochromator by Princeton Instruments equipped with a diffraction grating having 300 grooves per mm and blazed at 1 μm. The intensity of the dispersed light was measured by an InGaAs linear array detector (OMA-V, Roper Scientific) cooled at −100 °C.

3. Results and discussion

3.1. Optimization of the sulfurization conditions of $BaZrO_3$

The optimization of the sulfurization process was carried out on commercial $BaZrO_3$ powders (cubic crystal structure, space group $Pm\bar{3}m$, Fig. 1a and b). This first step is critical since the sulfurization of $BaZrO_3$ yields different phases depending on the chalcogen precursors (elemental S, H_2S or CS_2) and employed conditions (*e.g.*, open flow reactor or closed ampoules, sulfurization temperature and time).[17,18] Based on our previous experience, we chose CS_2 as sulfurization agent and explored the effect of sulfurization temperature – from 900 to 1100 °C – in closed ampoules (Fig. 1c). The chemical composition analysis carried out by EDX on the sulfurized powders reveals that the S/Ba and S/Zr ratios vary as a function of the sulfurization temperature (Fig. 1d and Fig. S1, ESI†). This trend agrees with the results obtained from XRPD analysis.

Indeed, the high oxygen and low sulfur contents (S/Ba and S/Zr ratios between 1.5 and 1.8) in the samples prepared at 900 and 950 °C follow from the presence of a mixture of crystalline phases: ZrO_2 (both in monoclinic and tetragonal phases) and

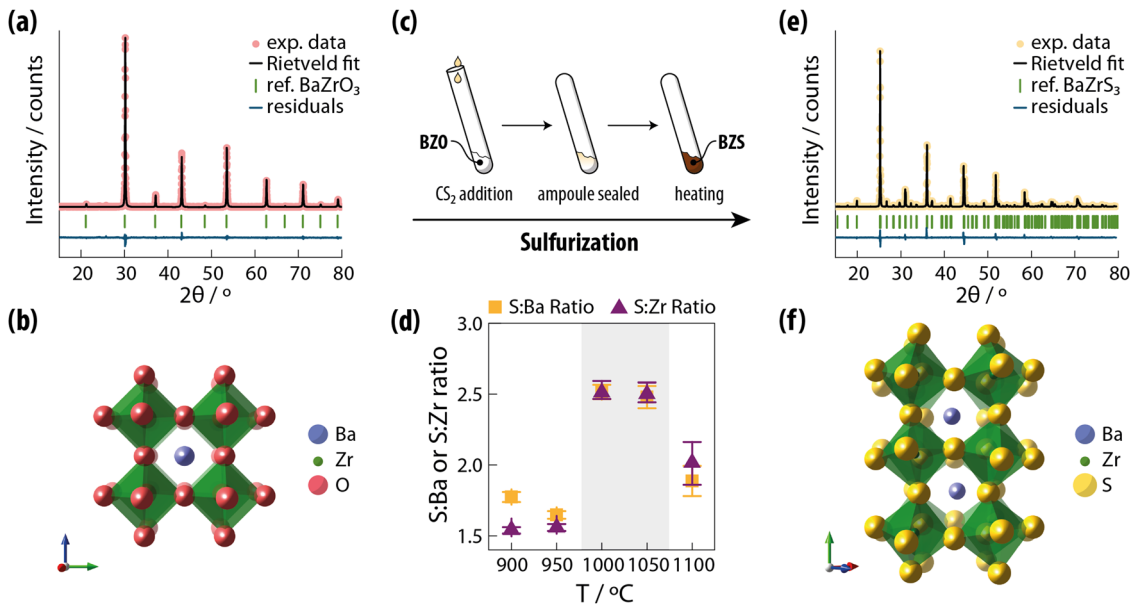

Fig. 1 (a) XRPD pattern of commercial BZO (red circles), its Rietveld refinement (black line), alongside the residuals (blue line) and the position of the Bragg reflexes for cubic $BaZrO_3$ (green vertical lines, JCPDS 96-153-2744). (b) Schematic crystal structure of cubic $BaZrO_3$. (c) Schematic representation of the sulfurization process of BZO with CS_2. (d) S/Ba and S/Zr ratios obtained by EDX analyses as a function of the sulfurization temperature. (e) XRPD pattern of BZS obtained from the sulfurization of BZO at 1000 °C (yellow circles), its Rietveld refinement (black line), alongside the residuals (blue line) and the position of the Bragg reflections for cubic $BaZrS_3$ (green vertical lines, JCPDS 01-073-0847). (f) Schematic crystal structure of $BaZrS_3$.

other unidentified phases (Fig. S2b and c, ESI†). These latter phases contain S according to EDX analyses (Fig. 1d and Fig. S1b, c, ESI†). However, the crystal structures of BZS-900 and BZS-950 are not the same, as evidenced by XRPD measurements and the different optical bandgaps observed in both samples (see Fig. S5, ESI†). The presence of unidentified phases when sulfurizing $BaZrO_3$ with CS_2 at 900 °C was also reported by Clearfield.[19]

The diffraction patterns of BZS-1000 and BZS-1050 can be indexed to a single $BaZrS_3$ phase with an orthorhombic distorted perovskite structure with space group *Pnma* (JCPDS 01-073-0847; Fig. 1e, f and Fig. S2d, e, ESI†). This phase features Zr^{4+} sites with distorted octahedra (B site) and Ba^{2+} in the higher-coordination A site, as it occurs for the parent $BaZrO_3$ compound (Fig. 1b and f). The S/Ba and S/Zr ratios in BZS-1000 and BZS-1050 were close to 2.5: A value indicative of a sub-stoichiometric sulfur content, and hence suggesting the presence of sulfur vacancies in the crystal structure. This off-stoichiometry has been previously observed in $BaZrS_3$ perovskites,[20,21] and mirrors the oxygen vacancies generally observed in $BaZrO_3$.[22]

Upon further increasing the sulfurization temperature to 1100 °C, the S/Ba and S/Zr ratios decrease to 1.8 and 2.1, respectively (Fig. 1d and Fig. S1f, ESI†) and the XRPD patterns reveal the presence of two crystalline phases (Fig. S2f, ESI†): a $Ba_3Zr_2S_7$ Ruddlesden–Popper phase (*Cccm*, JCPDS 01-080-1999) and monoclinic ZrO_2 ($P2_1/c$, JCPDS 01-078-1807). The appearance of $Ba_3Zr_2S_7$ phase at this sulfurization temperature has been also reported by Saeki *et al.*[23]

According to the above results, a temperature between 1000 and 1050 °C is thus optimal for the preparation of pure-phase $BaZrS_3$ *via* CS_2-assisted sulfurization of $BaZrO_3$. Therefore, these conditions were used to sulfurize Ln^{3+}-doped $BaZrO_3$ powders.

3.2. Suitability of $BaZrS_3$ as matrix for Ln^{3+}-doped phosphors

We subsequently investigated the vibrational modes of the parent $BaZrO_3$ and the sulfurized $BaZrS_3$ phases *via* Raman spectroscopy (Fig. 2a), observing a good match with the data reported in the literature.[21,24–29] Importantly, $BaZrS_3$ shows a higher density of phonon ($h\omega$) modes at lower energies compared to $BaZrO_3$. The more intense (*i.e.* statistically abundant) phonon modes in $BaZrS_3$ are found at energy values <400 cm^{-1}. In this regard, $BaZrS_3$ is similar to – if not better than – state-of-the-art low-phonon energy fluoride matrices used to prepare efficient Ln^{3+}-doped phosphors, like $NaYF_4$ and $LiYF_4$.[30–32] This consideration is pivotal in the context of Ln^{3+}-based phosphor preparation, since multiphonon relaxation (MPR) is a major contributor of photoluminescence quenching. The lower the $h\omega$ value featured by the matrix, the more phonons are required to non-radiatively depopulate Ln^{3+} excited states, thus maximizing the probability of radiative relaxation instead.[33]

The most noticeable change introduced by sulfurization is the change of the material color from white to dark brown (Fig. S4, ESI†). This is a result of the extension of the absorption range of the material (Fig. 2b), passing from a bandgap of (3.7 ± 0.1) to (1.77 ± 0.05) eV for $BaZrO_3$ and $BaZrS_3$, respectively (Fig. 2c). These values were extracted from diffuse reflectance spectra using the Kubelka–Munk methodology[34] considering direct allowed transitions, and they agree with reported data for $BaZrO_3$[3] and $BaZrS_3$.[35,36] This extension of the absorption range passing from oxide to sulfide sets the conditions for matrix-assisted visible sensitization of NIR emission of luminescent Ln^{3+} ions doped in $BaZrS_3$.

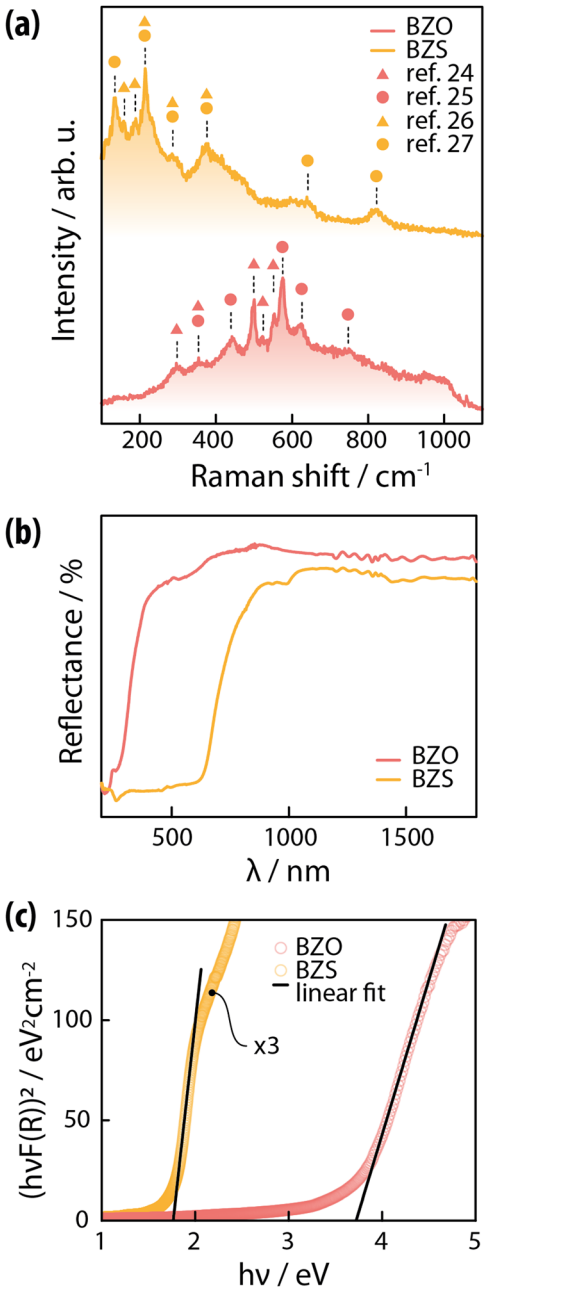

Fig. 2 (a) Raman spectra of commercial $BaZrO_3$ (BZO) and $BaZrS_3$ obtained after sulfurization of $BaZrO_3$ at 1000 °C (BZS-1000). Dotted lines are guidelines to follow the position of the different modes, and symbols indicate the previously reported Raman peak positions for BZO and BZS (red triangles,[24] red circles,[25] yellow triangles,[26] yellow circles[27]). (b) Diffuse reflectance spectra of BZO and BZS-1000 samples. (c) Tauc plots (direct allowed transitions) obtained from the corresponding Kubelka–Munk functions of BZO and BZS-1000 samples. The lines are the linear fits used to calculate the optical energy bandgaps.

Lastly, the stability of $BaZrS_3$ was studied. For that, TGA measurements were conducted under Ar atmosphere (Fig. S6a, ESI†), observing negligible weight loss (<0.1%) below 400 °C, and an overall excellent thermal stability up to 1000 °C, with a total weight loss below 1.4%. The XRPD pattern of the sample recorded after this analysis (Fig. S6b, ESI†) showed that the dominant phase was still $BaZrS_3$, although traces of other phases appeared, which might have formed by reaction with O_2 or CO_2 traces in the TGA setup and partial decomposition of the material. Previous results by Niu *et al.*[37] also showed the high stability of $BaZrS_3$ even when heated up to 500 °C in air. In addition, $BaZrS_3$ also presents excellent stability when stored in air for long periods, as evidenced from the comparison of XRPD patterns obtained from a fresh sample and after one year of storage in air (Fig. S7, ESI†). Despite a tendency to degrade when immersed in water (Fig. S8, ESI†), $BaZrS_3$ shows an overall good stability and is hence an ideal candidate for its use in lighting and, more generally, high-temperature applications.

3.3. Incorporation of Ln^{3+} ions into $BaZrS_3$

For the preparation of Ln^{3+}-doped $BaZrS_3$, we firstly synthesized Ln^{3+}-doped $BaZrO_3$ microparticles (Ln = Nd, Er, Yb) *via* a MW-assisted hydrothermal approach. This synthetic procedure yielded particles with a size of few micrometers and a deca-octahedral morphology (Fig. 3a, c, e, and Fig. S9, ESI†) that is typical of $BaZrO_3$ powders.[38] EDX analysis – conducted recording spectra from several particles of each sample – yielded the chemical compositions given in Table 1. Ba : (Zr + Ln) ratios close to 1 were observed for all the samples, while O : Ba ratios lower than 3 were encountered. These values underscore the presence of oxygen vacancies, which are usually observed in $BaZrO_3$.[22,39] The concentrations of Ln^{3+} were close to the nominal value of 2% (considering substitutional doping at the Zr^{4+} site), hence confirming the incorporation of the Ln^{3+} ions within the host $BaZrO_3$ matrix. Moreover, EDX mapping of the BZO-Ln samples reveal a homogeneous distribution of the different elements (including the Ln^{3+} ions) in the obtained powders (Fig. S10, ESI†). The diffraction patterns of all the samples can be indexed to a single perovskite $BaZrO_3$ phase with the expected cubic structure ($Pm\bar{3}m$; Fig. S12 and Table S1, ESI†). The crystal structure of the host material is thus preserved after incorporation of the Ln^{3+} ions, which are expected to mainly substitute Zr^{4+} ions at the octahedral site (B-site) coordinated by 6 O^{2-}.[3,12,13,40] However, some substitutional doping of Ln^{3+} ions in cuboctahedral Ba^{2+} sites (*i.e.*, A sites) can also occur.[11,39] The incorporation of Ln^{3+} ions (BZO-Ln) is accompanied by a slight shift of the diffraction peaks towards lower angles compared to undoped $BaZrO_3$ (BZO). Rietveld refinements of the diffraction patterns (Fig. S12, ESI†) show an expansion of the lattice parameter of the Ln^{3+}-doped samples compared to the undoped one (Table 1). This effect can be ascribed to the larger ionic radius of Ln^{3+} (98, 89 and 87 pm for Nd^{3+}, Er^{3+}, and Yb^{3+}, respectively) compared to Zr^{4+} (72 pm) in octahedral coordination.[41] Similar results have been previously reported for Ln^{3+}-doped $BaZrO_3$ samples.[12,13]

After confirming the successful incorporation of the Ln^{3+} ions in the oxide matrix, we sulfurized the materials – using the optimal conditions described in Section 3.1 – to obtain the

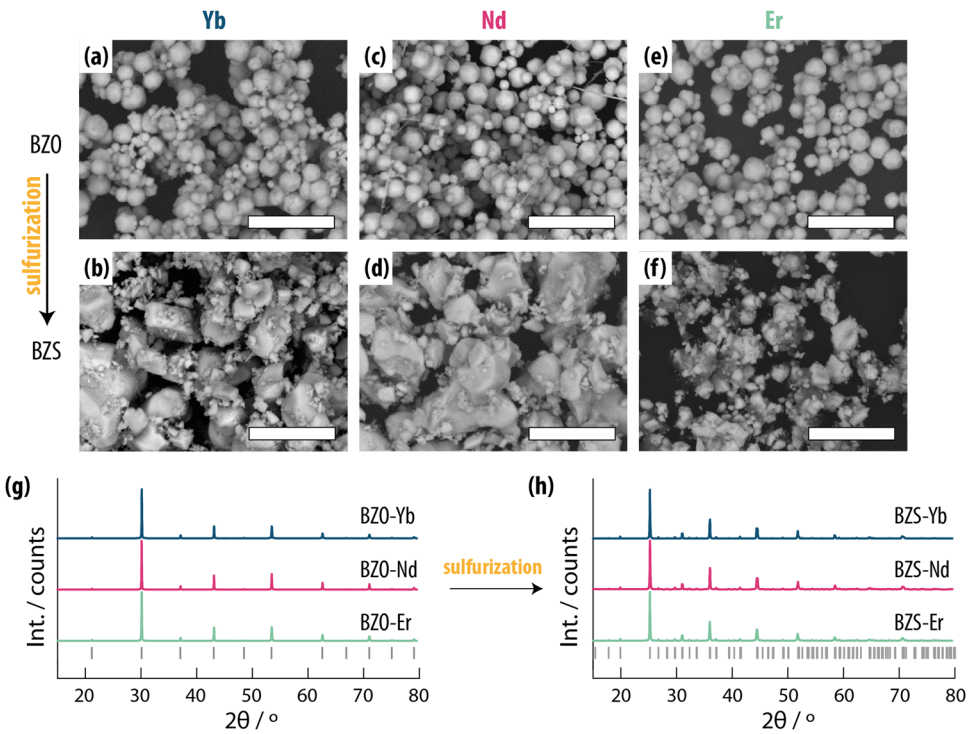

Fig. 3 SEM images of BZO-Yb (a), BZS-Yb (b), BZO-Nd (c), BZS-Nd (d), BZO-Er (e) and BZS-Er (f). Scale bars are 10 μm. XRD patterns of BZO-Ln series (g) and of BZS-Ln series (h). Vertical grey lines in (g) and (h), respectively indicate the position of the Bragg reflections for $BaZrO_3$ and $BaZrS_3$.

Table 1 Unit cell volumes obtained by Rietveld refinements of XRPD patterns and chemical compositions determined by EDX[a] for both undoped and Ln^{3+}-doped series of $BaZrO_3$ and $BaZrS_3$ samples

Sample name	V (Å^3)	Chemical composition	Sample name	V (Å^3)	Chemical composition
BZO	73.655	$Ba_{1.02}Zr_{1.00}O_{2.67}$	BZS-1000	495.08	$Ba_{0.99}Zr_{1.00}S_{2.50}$
BZO-Nd	73.732	$Ba_{1.11}Zr_{0.97}Nd_{0.03}O_{2.58}$	BZS-Nd	495.58	$Ba_{0.99}Zr_{0.98}Nd_{0.02}S_{2.43}$
BZO-Er	73.777	$Ba_{1.06}Zr_{0.98}Er_{0.02}O_{2.67}$	BZS-Er	497.04	$Ba_{0.94}Zr_{0.98}Er_{0.02}S_{2.60}$
BZO-Yb	73.790	$Ba_{1.06}Zr_{0.98}Yb_{0.02}O_{2.56}$	BZS-Yb	496.76	$Ba_{0.95}Zr_{0.99}Yb_{0.01}S_{2.50}$

[a] The uncertainty on the atomic concentrations measured by EDX is approximately 1 at%.

Ln^{3+}-doped $BaZrS_3$ phosphors. SEM images show that the decaoctahedral morphology exhibited by parent oxide particles was lost after sulfurization, with the sulfide particles being bigger and presenting an irregular shape (Fig. 3). This observation suggests that gaseous/liquid intermediates might form during the sulfurization process, which are subsequently deposited/solidified, thus producing irregular particles with a larger size.

The average chemical formulas determined from EDX analyses (Table 1) indicate a stoichiometry close to that of the expected $BaZrS_3$ phase yet sulfur-deficient (S/Ba $\approx$ 2.5), which is indicative of the presence of sulfur vacancies in the perovskite structure. Most crucially, the Ln^{3+} ions were retained in the lattice of the host matrix after sulfurization with a content comparable to that found in parent BZO-Ln powders. As in the case of the BZO-Ln samples, EDX maps obtained from the BZS-Ln particles show a homogeneous distribution of the composing elements in the samples (Fig. S11, ESI†). The diffraction patterns of all sulfurized samples presented a single crystalline phase characteristic of $BaZrS_3$. It is expected that Ln^{3+} remains at the B site (this time surrounded by 6 S rather than 6 O) after the sulfurization process. The retention of Ln^{3+} ions during the sulfurization is also supported by the results of the Rietveld analysis (Fig. S12 and Table S2, ESI†), which shows an increase in the cell volume upon incorporation of the Ln^{3+} ions in the crystalline structure (Table 1). This effect mirrors the one observed for the BZO-Ln series.

The occurrence of a $BaZrS_3$ perovskite structure in the BZS-Ln samples was further confirmed by Raman measurements (Fig. S13 and Table S3, ESI†). Moreover, the Raman spectra recorded on different particles were repeatable, thus highlighting a good homogeneity of the powders.

To summarize, we have shown that Ln^{3+}-doped $BaZrS_3$ perovskite microparticles can be prepared by sulfurization of the corresponding doped oxides.

3.4. Optical properties of $BaZrS_3$ doped with Ln^{3+} ions

We then moved to investigate the optical properties of BZS-Ln powders and their capability to support matrix-sensitized emission of the Ln^{3+} ions.

First, values of bandgap between 1.75–1.85 eV were extracted from the diffuse reflectance spectra of the BZS-Ln series (Fig. S14, ESI†), in agreement with the value obtained for the undoped sample (BZS, 1.77 eV). This broad, visible absorption of the matrix – characterized by an absorption coefficient $>10^4$ cm^{-1} above 2.0 eV[36] – is an important prerequisite for matrix-mediated sensitization of the NIR emission of the doped Ln^{3+} ions.

Subsequently, we investigated the emission of BZS and BZS-Ln powders under either 405 (3.06 eV) or 532 nm (2.33 eV) excitation (Fig. 4) focusing on the NIR wavelength range. The undoped material (BZS) displayed a broadband emission covering the 0.8–1.6 eV range when excited at 405 nm. Temperature-dependent photoluminescence measurements show a distinct quenching of the high- and low-energy side of the band, suggesting the presence of two radiative relaxation pathways. The high-energy deexcitation channel (centered at approximately 1.25 eV) is dominant at 10 K, while only the low-energy route (centered at approximately 1.10 eV) remains observable approaching room temperature. The presence of two emission components in the NIR range is consistent with the results reported by Márquez *et al.*[42] Note that both bands are located at energies well below the one expected for excitonic emission, considering a bandgap close to 1.8 eV. This observation hints at the involvement of localized, intra-bandgap energy states in the electronic transitions that underpin this luminescence signal. The nature of these states is not clear, yet, based on the results reported in the sections above, we hypothesize that they might be related to sulfur vacancies. The integrated intensity of the band *vs.* temperature was fitted according to the Mott–Seitz model[43,44] with two non-radiative components:

$$I = \frac{I_0}{1 + \alpha_1 \exp(-\Delta E_1/k_B T) + \alpha_2 \exp(-\Delta E_2/k_B T)} \quad (1)$$

where I_0 is the intensity at T = 0 K, α_i are weighing coefficients, ΔE_i are the activation barriers of the non-radiative relaxation mechanisms, and k_B is the Boltzmann's constant (the values of α_i and ΔE_i obtained from the fitting procedure of the datasets in Fig. 4c, e and g, and *i* are reported in Table S4, ESI†). Despite the qualitative nature of this approach, two distinct energy barriers for the quenching mechanisms were extracted from the fitting procedure: 20 and 161 meV (160 and 1300 cm^{-1}). These results suggest that the higher-energy emission component involves an intra-bandgap energy level shallower than the lower-energy one (Fig. 4c).

Upon doping the material with Ln^{3+} ions, the NIR photoluminescence changes drastically (Fig. 4d, f and h). To that end, BZS-Yb displays the expected Yb^{3+}:$^2F_{5/2} \rightarrow {}^2F_{7/2}$ emission band, while the intrinsic broad luminescence of the matrix completely disappears. Note that Yb^{3+} cannot be directly excited at 532 nm, moreover the emission of this ion in BZS-Yb is observed also under 405-nm excitation (Fig. S15, ESI†). These observations confirm the sensitization of Yb^{3+} emission upon excitation of the semiconductor matrix. Intriguingly, close inspection of the

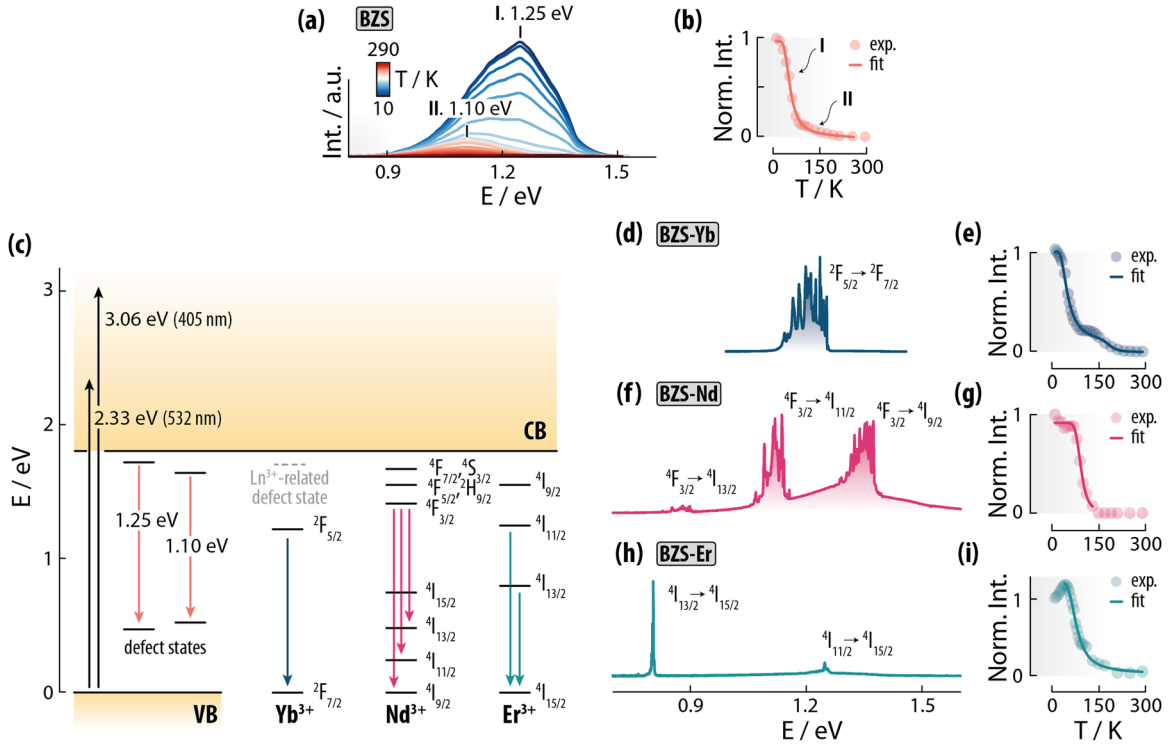

Fig. 4 (a) Photoluminescence of BSZ (undoped $BaZrS_3$) as a function of temperature and (b) intensity *vs.* temperature plot obtained integrating over the whole range shown in (a). (c) Proposed energy level scheme for the doped and undoped samples. For Ln^{3+} ions, only the energy levels that are in the range <1.8 eV are shown. The emission spectra recorded at 10 K for BZS-Yb, BZS-Nd, and BZS-Er are shown in (d), (f), and (h), alongside the intensity *vs.* temperature plots obtained for each sample – shown respectively in (e), (g), and (i). Details about the data treatment for obtaining the integrated intensity for (e), (g), and (i) can be found in the ESI.† All the fittings were carried out using eqn (1). All spectra were collected under 405-nm excitation, save for the BZS-Yb sample, which was excited at 532 nm.

Yb^{3+} emission band reveals more signals than the expected four Stark components even at 10 K, alongside a thermal quenching trend entailing at least two steps (Fig. 4e). This behaviour indicates that at the very least two populations of Yb^{3+} ions that are optically non-equivalent are present in the $BaZrS_3$ crystal structure (additional discussion on this topic can be found in the ESI†).

For BZS-Nd, we moved from 532 to 405-nm excitation. This is because Nd^{3+} can be directly excited with the former wavelength (green) but shows negligible absorption at the latter (violet). As such, the Nd^{3+} emission lines observed in BZS-Nd under 405-nm excitation are the result of energy transfer from the semiconductor matrix to the dopant ions. The NIR luminescence spectrum displayed by BZS-Nd is more complex than the one of BZS-Yb, featuring both the emission of the Ln^{3+} ion and broader bands that closely resemble the emission of the undoped material. Each contribution has a distinctive thermal quenching behaviour (Fig. 4g and Fig. S17, ESI†), possibly underscoring the presence of temperature-dependent (back) energy transfer mechanisms between the energy levels of Nd^{3+} and the ones of the matrix (Fig. 4c).

Lastly, BZS-Er was excited at 405 nm. Note that Er^{3+} is directly excited at this wavelength, leading to population of the $^2H_{9/2}$ excited state. Yet, the minimal contribution of the matrix luminescence (Fig. S18, ESI†) to the overall emission of BZS-Er suggest that the part of optical energy that is absorbed by the matrix is effectively funnelled to the dopant Er^{3+} ions (Fig. 4h). As in the previous Ln^{3+}-doped samples, a two-step thermal quenching of the PL signal is observed (Fig. 4i). This sample is also the only one showing anti-thermal quenching behaviour between 10 and 50 K. This trend is compatible with thermally-induced detrapping of charge carriers from (shallow) trap/defect states followed by capture by deeper emitting states – here belonging to Er^{3+}.[45]

Therefore, the typical NIR emission bands of each Ln^{3+} ion were observed under excitation of the host matrix. It is expected that substitutional doping of Zr^{4+} with Ln^{3+} ions is accompanied by the formation of additional sulfur vacancies due to charge compensation. For energetic reasons, these vacancies should reside in the proximity of the introduced Ln^{3+} ions, thus possibly supporting localized energy transfer processes. A similar phenomenon has been observed in Ln^{3+}-doped $CsPbCl_3$ nanocrystals, where 2 Ln^{3+} replace 3 Pb^{2+}, leaving an unoccupied site (Pb^{2+} vacancy, V_{Pb}); this localized, energetically favorable Ln–V_{Pb}–Ln defect complex appears to be fundamental in supporting, for example, efficient quantum cutting in Yb^{3+}-doped $CsPbCl_3$.[8] Modelling and additional experimental studies (*e.g.*, lifetime measurements) are required to pinpoint the exact nature of the semiconductor-to-Ln^{3+} transfer process in $BaZrS_3$.

4. Conclusions

We have herein reported the first example of Ln^{3+} ion doping into $BaZrS_3$ and matrix-to-Ln^{3+} near infrared (NIR) sensitized

emission. We prepared these phosphors *via* sulfurization of Ln^{3+}-doped $BaZrO_3$ powders, which were in turn obtained through a microwave-assisted strategy.

We initially investigated the optimal sulfurization conditions of $BaZrO_3$ to obtain pure-phase $BaZrS_3$. We observed that different phases can be obtained when varying the sulfurization temperature and determined an optimal range of sulfurization temperatures between 1000 and 1050 °C. The so-obtained $BaZrS_3$ presents good stability both at high temperature and at ambient conditions over time. Moreover, it features a band gap energy of approximately 1.8 eV, which ensures efficient visible light absorption. Not less importantly, $BaZrS_3$ presents low-energy phonon modes. All the above features set the conditions for the preparation of visible-excited, NIR-emitting Ln^{3+}-doped $BaZrS_3$ phosphors.

We therefore prepared $BaZrS_3$ phosphors doped with Nd^{3+}, Er^{3+}, and Yb^{3+} and investigated their NIR photoluminescence under violet and green light excitation. Characteristic emission lines of Nd^{3+}, Er^{3+} and Yb^{3+} ions were observed. The analysis of the photoluminescence spectra acquired as a function of the temperature (10 K to room temperature) on both doped and undoped samples shows a rich spectroscopy of these materials. Specifically, two broad, defect state-related, emission bands were observed alongside the sensitized narrow emission of each doped Ln^{3+} ion. These results pave the way towards future applications of perovskite sulfides as visible light absorbing phosphors and sensitizers of Ln^{3+} NIR emission, moving from the cryogenic range towards room temperature.

Data availability

Data for this article, including the original datasets of the X-ray powder diffraction, Raman, reflectance, Tauc plots, and photoluminescence (all in .txt format) are available at Zenodo at **https://doi.org/10.5281/zenodo.13937075**.

Conflicts of interest

There are no conflicts to declare.

Acknowledgements

The authors acknowledge the technical assistance of Mr F. Moreno, and the use of SIdI and Segainvex facilities at Universidad Autónoma de Madrid. This research has been funded by Spanish Ministerio de Ciencia, Innovación y Universidades (MICIU) under PID2021-126098OB-I00/AEI/FEDER10.13039/501100011033 grant. R. M. is also grateful to the Spanish MICIU for support to research through a Ramón y Cajal Fellowship (RYC2021-032913-I) and Project PID2022-14210NA-I00 (NAMSTEPS) funded by MICIU/AEI/10.13039/501100011033 and by FEDER, EU. A. B. acknowledges funding from Comunidad de Madrid (Spain) through TALENTO grants ref. 2019-T1/IND-14014 and ref. 2023-5A/IND-28937. A. P. and E. B. acknowledge support by Sapienza University of Rome (progetti medi 2022).

References

1 R. Marin, G. Brunet and M. Murugesu, Shining new light on multifunctional lanthanide single-molecule magnets, *Angew. Chem., Int. Ed.*, 2021, **60**, 1728–1746.
2 A. Satapathy and E. Sinha, Optical band gap and photoluminescence studies of samarium-doped barium zirconate perovskite prepared by solid state reaction route, *J. Appl. Spectrosc.*, 2018, **84**, 948–953.
3 R. Borja-Urby, L. Diaz-Torres, P. Salas, M. Vega-Gonzalez and C. Angeles-Chavez, Blue and red emission in wide band gap BaZrO3: Yb^{3+}, Tm3+, *Mater. Sci. Eng. B*, 2010, **174**, 169–173.
4 R. Marin and D. Jaque, Doping lanthanide ions in colloidal semiconductor nanocrystals for brighter photoluminescence, *Chem. Rev.*, 2021, **121**, 1425–1462.
5 W. J. Mir, T. Sheikh, H. Arfin, Z. Xia and A. Nag, Lanthanide doping in metal halide perovskite nanocrystals: spectral shifting, quantum cutting and optoelectronic applications, *NPG Asia Mater.*, 2020, **12**, 9.
6 A. G. Bispo-Jr, A. J. de Morais, C. M. S. Calado, I. O. Mazali and F. A. Sigoli, Lanthanide-doped luminescent perovskites: A review of synthesis, properties, and applications, *J. Lumin.*, 2022, **252**, 119406.
7 H. Shao, L. Li, X. Wu, L. Xu, B. Dong, D. Zhou, X. Bai and H. Song, Multicolor emission from lanthanide ions doped lead-free $Cs_3Sb_2Cl_9$ perovskite nanocrystal, *J. Rare Earths*, 2024, **42**, 940–946.
8 T. J. Milstein, D. M. Kroupa and D. R. Gamelin, Picosecond Quantum Cutting Generates Photoluminescence Quantum Yields Over 100% in Ytterbium-Doped $CsPbCl_3$ Nanocrystals, *Nano Lett.*, 2018, **18**, 3792–3799.
9 Y. Liang, J. Li, Z. Chen, G. Li, M. Li, M. Jia, X. Chen, X. Li, Y. Han and Z. Shi, Tapping the Light Emitting Potential of Chalcogenide Perovskite $SrHfS_3$ via Eu^{2+} Doping, *Adv. Optical Mater.*, 2024, **12**, 2301977.
10 Y. Han, J. Fang, Y. Liang, H. Gao, J. Yang, X. Chen, Y. Yuan and Z. Shi, Preparation of chalcogenide perovskite SrHfS3 and luminescent SrHfS3:Eu^{2+} thin films, *Appl. Phys. Lett.*, 2024, **124**, 131902.
11 D. Han, K. Shinoda and T. Uda, Dopant Site Occupancy and Chemical Expansion in Rare Earth-Doped Barium Zirconate, *J. Am. Ceram. Soc.*, 2014, **97**, 643–650.
12 R. Borja-Urby, L. Diaz-Torres, P. Salas, C. Angeles-Chavez and O. Meza, Strong broad green UV-excited photoluminescence in rare earth (RE = Ce, Eu, Dy, Er, Yb) doped barium zirconate, *Mater. Sci. Eng. B*, 2011, **30**, 1388–1392.
13 X. Liu and X. Wang, Preparation and luminescence properties of $BaZrO_3$: Eu phosphor powders, *Opt. Mater.*, 2007, **30**, 626–629.
14 R. Borja-Urby, L. A. Diaz-Torres, I. Garcia-Martinez, D. Bahena-Uribe, G. Casillas, A. Ponce and M. Jose-Yacaman, Crystalline and narrow band gap semiconductor $BaZrO_3$: Bi-Si synthesized by microwave-hydrothermal synthesis, *Catal. Today*, 2015, **250**, 95–101.
15 I. Leonidov, V. Tsidilkovski, E. Tropin, M. Vlasov and L. Putilov, Acceptor doping, hydration and band-gap engineering of $BaZrO_3$, *Mater. Lett.*, 2018, **212**, 336–338.

16 J. H. Al Shuhaib, J. F. Fernandez, J. Bodega, J. R. Ares, I. J. Ferrer and F. Leardini, Synthesis, optical band gap and thermoelectric properties of $Sr_{1+x}TiS_{3-y}$ chalcogenide perovskites, *Mater. Res. Bull.*, 2023, **167**, 112405.
17 C. Comparotto, A. Davydova, T. Ericson, L. Riekehr, M. V. Moro, T. Kubart and J. Scragg, Chalcogenide Perovskite BaZrS3: Thin Film Growth by Sputtering and Rapid Thermal Processing, *ACS Appl. Energy Mater.*, 2020, **3**, 2762–2770.
18 J. Xu, Y. Fan, W. Tian, L. Ye, Y. Zhang, Y. Tian, Y. Han and Z. Shi, Enhancing the optical absorption of chalcogenide perovskite $BaZrS_3$ by optimizing the synthesis and post-processing conditions, *J. Solid State Chem.*, 2022, **307**, 122872.
19 A. Clearfield, The Synthesis and Crystal Structures of some Alkaline Earth Titanium and Zirconium Sulfides, *Acta Cryst.*, 1961, **16**, 135–142.
20 S. Niu, H. Zhao, Y. Zhou, H. Huyan, B. Zhao, J. Wu, S. B. Cronin, H. Wang and J. Ravichandran, Mid-wave and Long-Wave Infrared Linear Dichroism in a Hexagonal Perovskite Chalcogenide, *Chem. Mater.*, 2018, **30**, 4897–4901.
21 X. Wei, *et al.*, Realization of BaZrS3 chalcogenide perovskite thin films for optoelectronics, *Nano Energy*, 2020, **68**, 104317.
22 T. S. Bjørheim, M. Arrigoni, S. W. Saeed, E. Kotomin and J. Maier, Surface Segregation Entropy of Protons and Oxygen Vacancies in $BaZrO_3$, *Chem. Mater.*, 2016, **28**, 1363–1368.
23 M. Saeki, Y. Yajima and M. Onoda, Preparation and Crystal Structures of New Barium Sulfides, *J. Solid State Chem.*, 1991, **92**, 286–294.
24 C. Toulouse, *et al.*, Lattice dynamics and Raman spectrum of $BaZrO_3$ single crystals, *Phys. Rev. B*, 2019, **100**, 134102.
25 D.-H. Gim, Y. Sur, Y. H. Lee, J. H. Lee, S. Moon, Y. S. Oh and K. H. Kim, Pressure-Dependent Structure of $BaZrO_3$ Crystals as Determined by Raman Spectroscopy, *Materials*, 2022, **15**, 4286.
26 S. Perera, *et al.*, Chalcogenide perovskites – an emerging class of ionic semiconductors, *Nano Energy*, 2016, **22**, 129–135.
27 N. Gross, Y.-Y. Sun, S. Perera, H. Hui, X. Wei, S. Zhang, H. Zeng and B. A. Weinstein, Stability and Band-Gap Tuning of the Chalcogenide Perovskite $BaZrS_3$ in Raman and Optical Investigations at High Pressures, *Phys. Rev. Appl.*, 2017, **8**, 044014.
28 J. Pandey, D. Ghoshal, D. Dey, T. Gupta, A. Taraphder, N. Koratkar and A. Soni, Local ferroelectric polarization in antiferroelectric chalcogenide perovskite $BaZrS_3$ thin films, *Phys. Rev. B*, 2020, **102**, 205308.
29 S. P. Ramanandan, *et al.*, Understanding the growth mechanism of $BaZrS_3$ chalcogenide perovskite thin films from sulfurized oxide precursors, *J. Phys. Energy*, 2023, **5**, 014013.
30 G. Chen, C. Yang and P. N. Prasad, Nanophotonics and Nanochemistry: Controlling the Excitation Dynamics for Frequency Up- and Down-Conversion in Lanthanide-Doped Nanoparticles, *Acc. Chem. Res.*, 2013, **46**, 1474–1486.
31 P. Loiko, *et al.*, Emission properties of Tm^{3+}-doped CaF_2, KY_3F_{10}, $LiYF_4$, $LiLuF_4$ and BaY_2F_8 crystals at 1.5 μm and 2.3 μm, *J. Lumin.*, 2020, **225**, 117279.
32 R. Shi and A.-V. Mudring, Phonon-Mediated Nonradiative Relaxation in Ln3 + -Doped Luminescent Nanocrystals, *ACS Mater. Lett.*, 2022, **4**, 1882–1903.
33 M. Szalkowski, M. Dudek, Z. Korczak, C. Lee, L. Marciniak, E. M. Chan, P. J. Schuck and A. Bednarkiewicz, Predicting the impact of temperature dependent multi-phonon relaxation processes on the photon avalanche behavior in Tm3 +: NaYF4 nanoparticles, *Optical Mater.: X*, 2021, **12**, 100102.
34 G. Kortum, W. Braun, D. Chem and G. Herzog, Principles and Techniques of Diffuse-Reflectance Spectroscopy, *Angew. Chem., Int. Ed. Engl.*, 1963, **2**, 333–341.
35 S. Niu, *et al.*, Bandgap Control via Structural and Chemical Tuning of Transition Metal Perovskite Chalcogenides, *Adv. Mater.*, 2017, **29**, 1604733.
36 Y. Nishigaki, *et al.*, Extraordinary Strong Band-Edge Absorption in Distorted Chalcogenide Perovskites, *Sol. RRL*, 2020, **4**, 1900555.
37 S. Niu, J. Milam-Guerrero, Y. Zhou, K. Ye, B. Zhao, B. C. Melot and J. Ravichandran, Thermal stability study of transition metal perovskite sulfides, *J. Mater. Res.*, 2018, **33**, 4135–4143.
38 M. L. Moreira, J. Andrés, J. A. Varela and E. Longo, Synthesis of Fine Micro-sized $BaZrO_3$ Powders Based on a Decaoctahedron Shape by the Microwave-Assisted Hydrothermal Method, *Cryst. Growth Des.*, 2009, **9**, 833–839.
39 P. G. Sundell, M. E. Björketun and G. Wahnström, Thermodynamics of doping and vacancy formation in $BaZrO_3$ perovskite oxide from density functional calculations, *Phys. Rev. B*, 2006, **73**, 104112.
40 I. Ahmed, S.-G. Eriksson, E. Ahlberg, C. S. Knee, H. Götlind, L.-G. Johansson, M. Karlsson, A. Matic and L. Börjesson, Structural study and proton conductivity in Yb-doped $BaZrO_3$, *Solid State Ion.*, 2007, **178**, 515–520.
41 R. D. Shannon, Revised Effective Ionic Radii and Systematic Studies of Interatomic Distances in Halides and Chalcogenide, *Acta Cryst.*, 1976, **A32**, 751–767.
42 J. A. Márquez, *et al.*, $BaZrS_3$ Chalcogenide Perovskite Thin Films by H2S Sulfurization of Oxide Precursors, *J. Phys. Chem. Lett.*, 2021, **12**(8), 2148–2153.
43 R. W. Gurney and N. F. Mott, Luminescence in solids, *Trans. Faraday Soc.*, 1939, **35**, 69–73.
44 F. Seitz, An interpretation of crystal luminescence, *Trans. Faraday Soc.*, 1939, **35**, 74–85.
45 P. Dang, W. Wang, H. Lian, G. Li and J. Lin, How to Obtain Anti-Thermal-Quenching Inorganic Luminescent Materials for Light-Emitting Diode Applications, *Adv. Opt. Mater.*, 2022, **10**, 2102287.

